Volume 9 | Number 1 | 7 January 2017 | Pages 1–466

Nanoscale

rsc.li/nanoscale

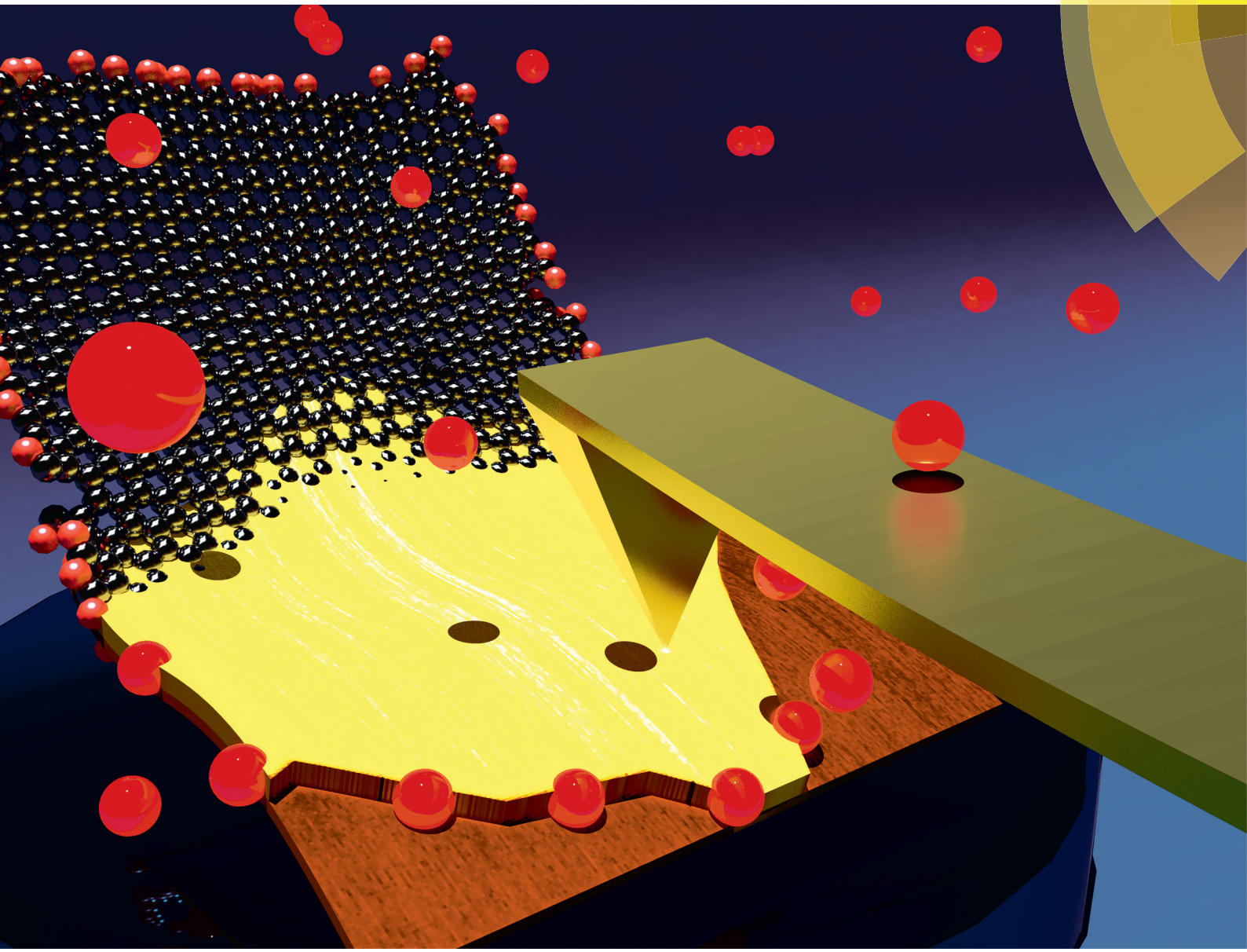

ISSN 2040-3372

ROYAL SOCIETY OF CHEMISTRY

PAPER

Mingdong Dong, Radek Zbořil, Michal Otyepka *et al.*

Direct mapping of chemical oxidation of individual graphene sheets through dynamic force measurements at the nanoscale

NCNST

Nanoscale

PAPER

View Article Online
View Journal | View Issue

Cite this: *Nanoscale*, 2017, **9**, 119

Direct mapping of chemical oxidation of individual graphene sheets through dynamic force measurements at the nanoscale†

Jens P. Froning,[a,b] Petr Lazar,[a] Martin Pykal,[a] Qiang Li,[b] Mingdong Dong,*[b] Radek Zbořil*[a] and Michal Otyepka*[a]

Received 22nd July 2016,
Accepted 26th September 2016

DOI: 10.1039/c6nr05799c

www.rsc.org/nanoscale

Graphene oxide is one of the most studied nanomaterials owing to its huge application potential in many fields, including biomedicine, sensing, drug delivery, optical and optoelectronic technologies. However, a detailed description of the chemical composition and the extent of oxidation in graphene oxide remains a key challenge affecting its applicability and further development of new applications. Here, we report direct monitoring of the chemical oxidation of an individual graphene flake during ultraviolet/ozone treatment through *in situ* atomic force microscopy based on dynamic force mapping. The results showed that graphene oxidation expanded from the graphene edges to the entire graphene surface. The interaction force mapping results correlated well with X-ray photoelectron spectroscopy data quantifying the degree of chemical oxidation. Density functional theory calculations confirmed the specific interaction forces measured between a silicon tip and graphene oxide. The developed methodology can be used as a simple protocol for evaluating the chemical functionalization of other two-dimensional materials with covalently attached functional groups.

Introduction

Graphene[1–3] possesses a unique application potential, such as in electronic devices,[4,5] sensors[6,7] and lithium ion batteries,[8,9] owing to its remarkable electronic properties. The functionalization of pristine graphene by chemical and physical methods is crucial for broadening its application range by generating new properties.[10] For instance, oxidized graphene or graphene oxide (GO) is more reactive than graphene[11–15] and highly water-dispersible,[16,17] making it a promising scaffold material for drug delivery,[18] sensing,[19,20] catalysis,[21,22] imaging,[23–25] substrates for implants[26] and low-cost production of large quantities of graphene and graphene-based materials.[27–29]

GO is a structurally complex material whose nature depends on the oxidation method used.[30] The surface of GO consists of randomly dispersed graphitic and oxidized regions covered by epoxy and hydroxyl groups. Other functional groups, such as carboxyl, quinone, ketone and peroxide, may also be present.[12,31,32] Owing to its random structural defects and plethora of possible functional groups, theoretical and experimental studies of GO's electronic properties, topography and reactivity are usually very complicated. Moreover, the monitoring of processes and changes gradually developing during graphene oxidation is highly challenging. Currently, most of the experimental techniques available to address this issue at the nanoscale resolution are hampered by considerable limitations. Scanning electron microscopy (SEM), high resolution transmission electron microscopy (HRTEM) and ultra-high vacuum scanning tunneling microscopy (UHV-STM) operate only in a vacuum. Ambient scanning tunneling microscopy (STM) requires a certain conductivity of the sample, which is limited for GO. Atomic force microscopy (AFM) phase-imaging can map the surface's interaction potential, but the interpretation is complicated.[33,34] Furthermore, the cantilever can jump between different oscillation states and interaction regimes causing different phase readings for the same material (see the ESI† for further discussion).[35] Other techniques, *e.g.*, Raman spectroscopy, X-ray photoelectron spectroscopy (XPS) and electrochemical approaches, lack the necessary nanometer-scale resolution. Kulkarni *et al.* showed prior to this work, electrostatic force microscopy could be used to identify reducing oxidation by alternating the

[a]*Regional Centre of Advanced Technologies and Materials (RCPTM), Department of Physical Chemistry, Palacký University Olomouc, Olomouc 78371, Czech Republic. E-mail: michal.otyepka@upol.cz, radek.zboril@upol.cz*
[b]*Interdisciplinary Nanoscience Center (iNANO), Aarhus University, Aarhus C 8000, Denmark. E-mail: dong@inano.au.dk*

† Electronic supplementary information (ESI) available: Further details regarding the measurement, UV/ozone treatment, adhesion measurement, graphene height characterization, detailed sample preparation, flow chart of the measurement, PeakForce mode, environmental stabilization and Raman spectra of treated samples. See DOI: 10.1039/c6nr05799c

surface potential,[36] further the oxidation on a single-layer graphene can also be measured through conventional force measurements. Ding *et al.*[37] showed a relationship between adhesion and graphene oxidation by standard force spectroscopy at a single point, demonstrating that force spectroscopy is a valid technique for monitoring oxidation alterations. However, the resolution of the force map is poor and the measurements are very time consuming. To overcome this limit, dynamic force mapping (DFM)[24,38,39] has been developed, which is able to record the morphology and quantitatively measure mechanical properties of nanomaterials simultaneously with the nanoscale resolution.[40] For DFM, the instrument collects several thousands of force spectra per second along with their *xy* positions to complete the surface mapping, while the indention depth is controlled to avoid plastic deformation of the probe and/or the surface (an example is given in the ESI†). A comparison of this mode with other AFM modes can be found in a review by Zhang *et al.*[33]

In this study, we report direct monitoring of the stepwise chemical oxidation of the same individual graphene flake during ultraviolet (UV)/ozone treatment, a known oxidation method,[41,42] through a combination of *in situ* AFM based DFM and density functional theory (DFT) calculations. By performing DFM measurements to record the interaction force map and topography of the same flake, we showed experimentally the difference between functionalization susceptibility of graphene surfaces and edges, which was examined theoretically by reactive molecular dynamics (MD) simulation. In addition, small alterations caused by the treatment, but hardly seen in XPS, were detected by fast DFM measurements through nanoscale interaction forces. Furthermore, interaction force mapping on the same graphene flake revealed that the oxidation spreads from the graphene edges across the entire surface. This was deducted, since we saw a clear correlation between the degree of oxygen functionalization determined by X-ray photoelectron spectroscopy (XPS) and force mapping of both the graphene flake and supporting SiO_2 substrate. The approach presented here could be used as a simple protocol for evaluating the chemical functionalization of other two-dimensional materials, such as transition metal dichalcogenides, carbon-based materials and flake–substrate composites.

Results and discussion

Computer simulation of the oxidation

Molecular dynamics simulation with a reactive force field was employed to simulate chemical changes of graphene upon oxidation. In the simulated oxidation, we utilized a non-periodic graphene sheet of 4 × 4 nm either uncapped or capped by hydrogen atoms, which was surrounded by atomic oxygen in a rectangular simulation box (Fig. 1(a)). Oxygen-containing groups replaced some of the hydrogens on the capped edges, whereas the uncapped edges were fully saturated with various

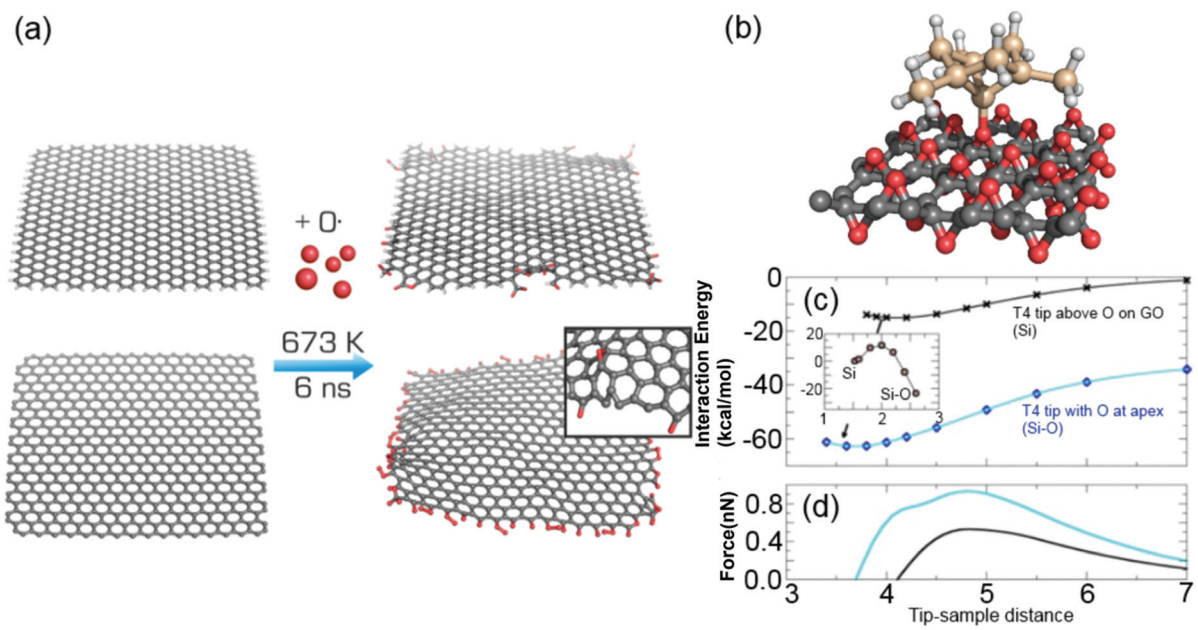

Fig. 1 Illustration of models used in the theoretical simulations. (a) The oxidation of graphene (shown capped by hydrogen atoms in the upper panel and uncapped in the lower panel) by atomic oxygen (in red; unbound oxygen atoms are not shown for clarity) was modeled by a 6 ns-long reactive MD simulation. The inset shows details of the edge and an epoxy group on the basal plane. (b) Model of a silicon T4 tip placed directly above an oxygen atom on GO. Carbon atoms are depicted in gray, oxygen in red, silicon in light brown and hydrogen in white. (c) Plot of the interaction energy between a T4 tip and GO. (d) The respective tip–surface force for the same T4 tip. The bare tip interacts rather weakly (black curve), but an oxygen atom can jump from GO to the tip and form a strong bond with a Si atom, which leads to sudden increase of the interaction force (blue curve). The inset in (c) shows the energy profile for the displacement of an O atom from GO to the T4 tip.

oxygen-containing functional groups in accordance with recent electrochemical observations.[30] Migration of oxidation onto the basal plane was only rarely observed, with only two events per whole simulation set.

Interaction forces between a model of an AFM silicon tip and both pristine and oxidized graphene were simulated by DFT calculations. Specifically, interactions between a T4 Si tip (see Methods for definition) and pristine graphene, oxygen-saturated GO or a SiO_2(0001) surface were evaluated. The interaction energy between the T4 Si tip and graphene was −24.6 kcal mol^{-1}, with an equilibrium distance from the plane to the tip apex of 2.7 Å (Fig. 1(b)). The simulated interaction force (0.8 nN) between the silicon probe and graphene was in agreement with a previous experimental report[43] (0.7 ± 0.2 nN), as well as a theoretical study by Ondráček *et al.*,[44] who obtained an interaction force of 0.7 nN for a T4 tip interacting with a single wall carbon nanotube. The calculations revealed that the tip–graphene interaction was of weak non-covalent character dominated by van der Waals interaction. For GO, the tip apex atom was at first placed among the oxygen atoms in GO. The calculated interaction energy and force with GO was weaker, *i.e.*, −17.9 kcal mol^{-1} and 0.7 nN, respectively. Similarly to graphene, the probe–GO interaction consisted mainly of van der Waals forces, and there was no covalent bonding between the probe and sample. Owing to the absence of covalent interactions at both graphene and GO, it was predicted that there would be no abrupt change of the interaction force caused by the oxidation of graphene. The interaction strength for the SiO_2 substrate was the same as for GO (0.7 nN), suggesting that there would be a lack of adhesion contrast between these two materials. It should be noted that we used dimer reconstruction[45] as a model of the SiO_2(0001) surface and reconstruction saturated the dangling bonds of surface oxygen atoms.

The simulation also revealed that the tip apex may be modified by absorption of single oxygen atoms from the GO surface in an exothermic process. This configuration with a relocated O atom (denoted as O-T4) was by 41.9 kcal mol^{-1} more stable than for a bare tip and surface (Fig. 1(c)). The energy barrier for O detachment from GO was 11.5 kcal mol^{-1} for the tip at an equilibrium distance of 4.2 Å (inset of Fig. 1(c)). The migration of oxygen to the tip created an oxygen vacancy at the GO surface and increased the interaction force to 0.9 nN (Fig. 1(c)) at this vacancy site. However, when the O-T4 tip was placed above one of the remaining O atoms on GO, a repulsive force between the tip apex O atom and the surface oxygen atom appeared, causing the tip's oxygen atom to bend sideways. This repulsion led to a shallow minimum in the interaction energy with a weak interaction force at 0.3 nN. This indicates that oxygen contamination of the Si tip weakened the adhesion forces and made the tip more sensitive to the surface defects and irregularities.

Dynamic force mapping of oxidation

The average chemical composition of the mechanically exfoliated graphene after UV/ozone treatment was verified using XPS by survey and high-resolution spectra (Fig. 2(a)–(d)). The UV/ozone treatment[41,42] allowed modifying the flake after deposition without the need to remove it. In this way alterations to the same flake could be monitored and it provided a reliable sample condition for the DFM measurements. Even during a relatively short time of oxidation, the relative oxygen and silicon content of the surface increased, whereas the amount of carbon decreased (Fig. 2(e)) due to the UV/ozone cleaning process releasing volatile CO*n* molecules. The oxidizing agent, ozone, primarily affected the carbon flake, since the O/Si ratio remained constant but the O/C ratio increased with each treatment cycle (Fig. 2(d)). The O/C ratio, which can be considered as an atomic coverage of graphene by oxygen, seemed to reach a saturation point where carbon oxidation and removal of carbon balanced each other,[41] as evident by the increasing number of defects in the AFM signal (further details regarding treatment times in the ESI†) and decrease in the total atomic signal of carbon (Fig. 2(e)).

The AFM based dynamic force spectroscopy measurements on graphene did not show any influence of a water layer in the force spectra as a result of increased hydrophilicity. The constant measurement conditions (humidity) were carefully carried out. However, the existence of a water layer cannot be ruled out. The chemical modification of the surface certainly will have an impact on water binding. Under the same humidity, the edge of graphene is significantly stronger than the surface of graphene. So, one can confirm that the adhesion must be due to the chemical modification (further details in the ESI†). The height of the untreated graphene flake was estimated to be 0.62 ± 0.07 nm above the SiO_2 substrate by AFM (Fig. S-3 in the ESI†). The step height from the single layer to double layer graphene was 0.42 ± 0.07 nm at places where the flake was folded back on itself, which is in accordance with the reported spacing of layers in the double layer graphene.[1]

AFM dynamic force mapping clearly revealed how the adhesion (Fig. 3(a) and (b)) and its contrast for the same graphene flake changed after the first minute of UV/ozone treatment (Fig. 3(d) and S-4 in the ESI†). The interaction force was higher in the experiment than in the simulation as a consequence of the increased area of interaction,[46–48] since actual AFM probes are usually not atomically sharp as presumed in the simulation. The first oxidation cycle of graphene by UV/ozone treatment (Fig. 3(c)) had no effect on the topography but caused pronounced changes in the total adhesion (Fig. 3(a) and (b)) and lower adhesion at the flake edge. This indicates a different degree of oxidation at the edges and on the surface. A higher oxidation activity at the graphene edges is in line with our MD simulation, as well as other studies showing that the edges are more reactive and prone to adsorption than the basal planes.[49–51] Additionally, the contrast was higher at places where the flake was folded back on itself. We hypothesized that bent graphene is probably more susceptible to oxidation than flat graphene. In line with this, Park, Srivastava, and Cho have studied the chemical reactivity as a function of the bending angle of carbon nanotubes and found

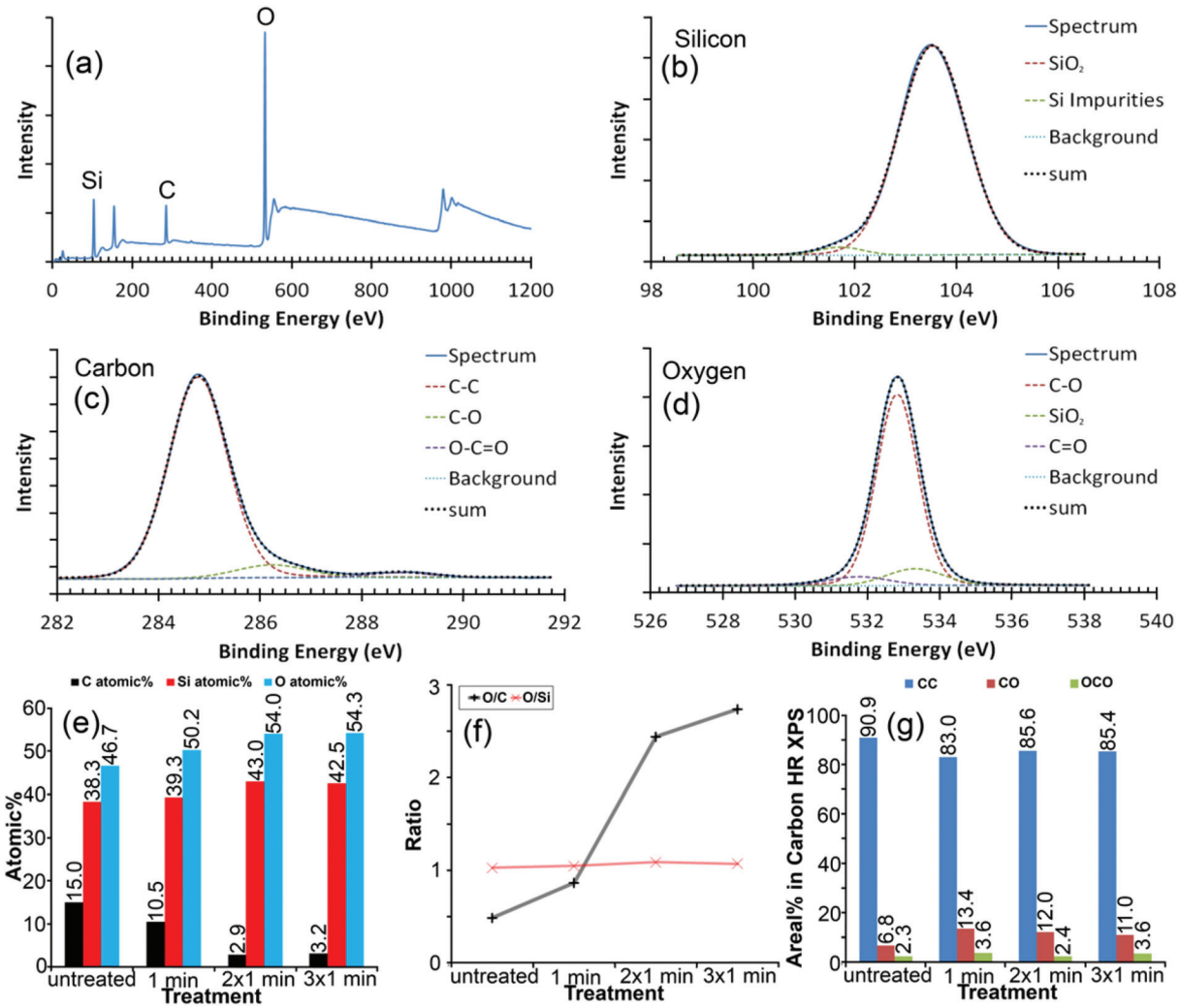

Fig. 2 XPS measurements of graphene flakes on a SiO_2 support illustrated by examples of (a) survey spectra, and high-resolution spectra of (b) 2p silicon, (c) 1s carbon and (d) 1s oxygen for untreated graphene on a SiO_2 substrate. Panel (e) shows the total atomic % ratios of C, O and Si for untreated and UV/ozone treated (for 1, 2 × 1 and 3 × 1 minutes) graphene determined from corrected areas of corresponding XPS peaks. Panel (f) shows the change in O/C and O/Si atomic % ratios during stepwise oxidation of graphene by UV/ozone treatment to illustrate the oxygen content development on graphene and the substrate. Panel (g) presents the ratios of various chemical forms of oxygen obtained from fitting 1s carbon high-resolution XPS spectra, showing that the values tended to become constant after the first round of oxidation.

that the hydrogenation energy was significantly enhanced in the kink area.[52]

Further oxidation (2 × 1 min) weakened the differences in contrast between the edge and the basal plane of the flake. The region of lower adhesion spread to the center of the flake but without noticeable differences in topography compared to untreated graphene (Fig. 3(c) untreated and 2 × 1 min). The contrast changed smoothly from the edge to the center of the flake, indicating that the oxidation gradually expanded over the whole flake. After the last treatment cycle (Fig. 3(d) 3 × 1 min), the adhesion contrast between the flake and substrate was inverted and several large defects appeared in both the topography and adhesion force images. The Root Mean Square (RMS) roughness of the graphene flake, 0.26 ± 0.03 nm according to ISO 4287/1-1997, hardly altered in the first two steps of treatment, being 0.23 ± 0.03 nm. After the last treatment, the roughness is nearly doubled, 0.47 ± 0.03 nm. This behavior causes an increased error in the adhesion, but the adhesion itself does not seem to be influenced. Through mapping, the bigger error is attributable to a higher adhesion at the defects (see Fig. 3), and shows the clear advantage of DFM mode over simple force spectroscopy.

We compared XPS results directly to the total adhesion and adhesion difference for a sharp silicon probe between SiO_2 and graphene (Fig. 4). Both the graphene flake and SiO_2 substrate were altered by the treatment since their total adhesion forces showed similar behavior (Fig. 4(a)). The adhesion forces increased strongly after the first treatment cycle and decreased slightly after the second treatment cycle, where each cycle lasted 1 min. After the third treatment cycle, total adhesion

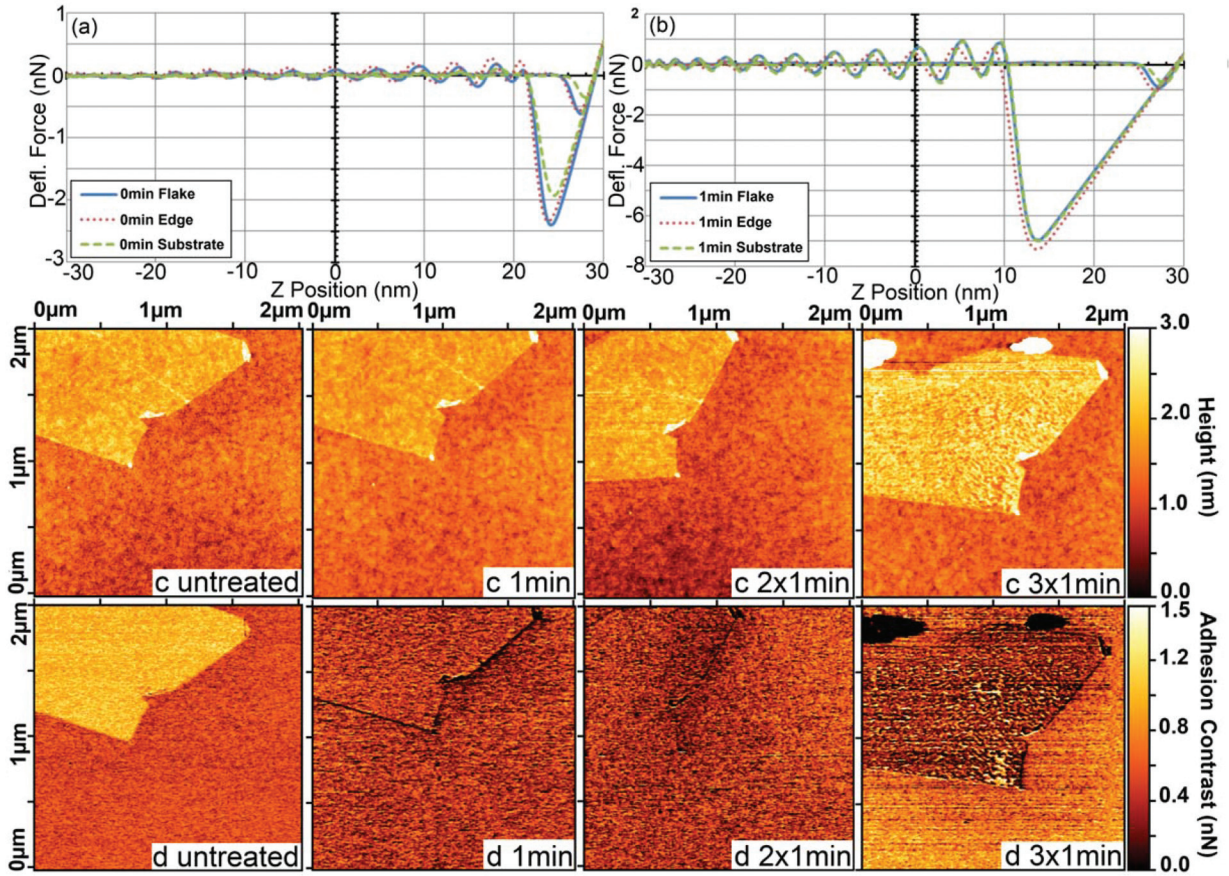

Fig. 3 Mapping of topography and interaction force by AFM. (a) Force spectra of untreated sample (0 min) and (b) 1 min treated sample at three different locations: on graphene surface, graphene edge and the support. Image series of the same graphene flake showing changes of (c) topography and (d) adhesion contrast during treatment. To aid illustration of the adhesion contrast development, the scale of the color bar has been kept constant for each channel, *i.e.*, height and adhesion contrast, in the two picture series, while the origin for each individual picture was set as the lowest measured value of each mapping.

alterations were hardly noticeable. This trend correlated with the degree of functionalization (DF), which was calculated from high resolution XPS data for the carbon peak as the fitted area of oxygen-containing bonds divided by the area related to the carbon–carbon bond signal (Fig. 2(c) and 4(a)). It should be noted that the XPS data did not reveal any significant chemical modifications of the SiO_2 film, in clear contrast to our force measurements, which might indicate either the reconstruction of the SiO_2 surface by UV[53] or a change of the entire sample surface for example by the increased hydrophilicity of both SiO_2 and graphene.

Fig. 3 illustrates how the adhesion contrast changed due to the treatment. In Fig. 4(b), we examined the difference in adhesion between the flake and substrate by subtracting the two respective adhesion values. This adhesion difference showed a clear trend that closely followed the C/O ratio on graphene. The adhesion difference reached a plateau because the average adhesion value measured after 3 min oxidation was affected by defects appearing on the graphene flake due to the UV/ozone treatment (Fig. 3(c) and (d)). Since the adhesion difference decreased with increased oxidation, it is plausible that the regions of lower adhesion after the second treatment cycle were caused by a higher degree of oxidation (Fig. 3(c) and (d)) (additional measurements with a spherical probe can be found in the ESI†).

Combining results for Fig. 3 and 4, we see a lower contrast means higher oxidation. In other words, the brim of graphene flakes and edges of graphite are more reactive and easier to oxidize than the basal plane. However, once the edge sites are saturated by oxygen atoms, the basal plane becomes more susceptible to oxidation. This mechanism was confirmed by the spreading of higher oxidized regions from the edge to the center of the flake during the treatment (Fig. 3(d)). This observation is consistent with the literature regarding similar carbon materials.[54] A plausible explanation is that the edge as a defect acts as a seed for further oxidation. The replacement and relief of the carbon atom defects in the graphene grid, allow further oxidation of the flake from the edge in a domino effect like fashion. Since the effect starts at the edge, the minimal size for the defect seems to be a vacant position in the carbon grid.

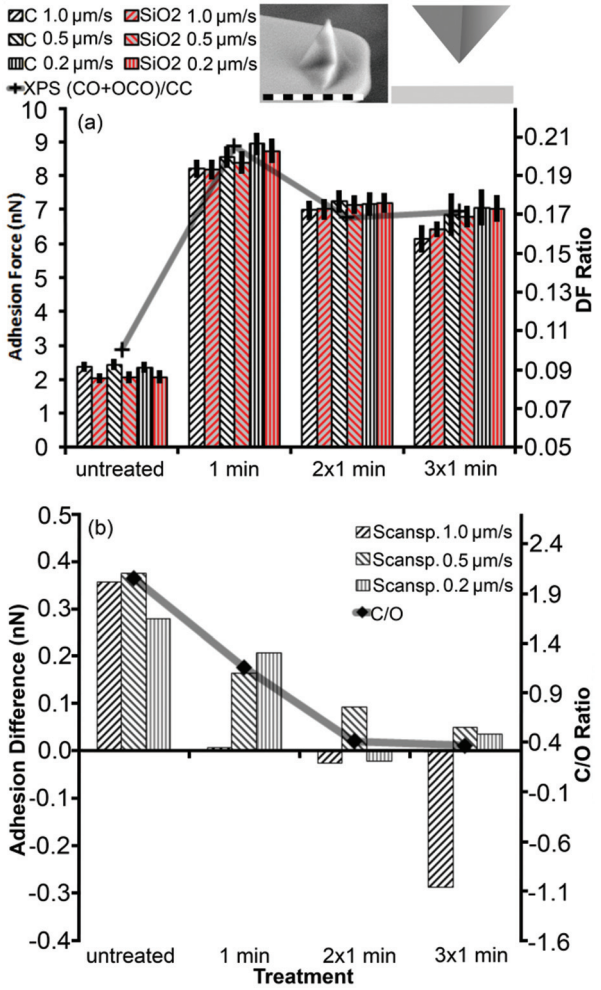

Fig. 4 Adhesion measurements acquired with a sharp probe on the same sample between UV/ozone treatments compared to XPS measurements. (a) Total adhesion force to graphene (black columns) and SiO_2 (red columns) measured at different scan speeds with a sharp probe (see SEM, scale bar equals 10 µm, and scheme of the AFM tip in inset) *vs.* treatment. The adhesion is directly compared to the degree of functionalization calculated from XPS (gray line). (b) Adhesion difference between the substrate and flake shown together with the C/O ratio obtained from XPS for all samples. Note: the C/O ratio is a different way to consider the functionalization of graphene based on atomic ratios instead of considering chemical groups on graphene used to obtain the degree of functionalization, "XPS (CO + OCO)/CC", shown in (a).

Methods

Theoretical calculations

The process of graphene oxidation was simulated using the ReaxFF reactive force field. ReaxFF is a bond-order dependent potential that has been shown to successfully describe bond formation and bond breaking in hydrocarbon–oxygen containing systems.[55] The force field parameters for the MD simulations were chosen to match known parameters for the structural evolution of GO during thermal annealing.[56] We considered a non-periodic 4 × 4 nm graphene sheet, either uncapped or capped with hydrogen atoms, that was immersed in a rectangular simulation box (8 × 8 × 8 nm) with atomic oxygen corresponding to an oxygen gas density of 0.16 g cm^{-3}. All simulations were carried out using the LAMMPS program package[57] in the NVT ensemble using the Nose/Hoover thermostat with 1 ps damping constant. The system was minimalized and heated from 10 K to the desired temperatures. Because the studied reactions were expected to occur on a timescale larger than accessible with present computational facilities, we ran our simulations at 473, 673 and 873 K increasing the collision frequency. All simulations were performed with a time step of 0.1 fs and the total length of simulations was 6 ns.

DFT calculations were performed using the projector-augmented wave method in the Vienna *ab initio* simulation package (VASP) suite.[58,59] The energy cutoff for the plane-wave expansion was set to 400 eV. The interaction energy and forces were calculated by applying the optimized van der Waals functional optB86b-vdW,[60] which has been shown to satisfactorily cover both local and non-local electron–electron correlation effects, including London dispersive forces.[61,62] The optB86b-vdW functional was shown to produce excellent results in a recent study of the adsorption of organic molecules on graphene.[63] The forces between the surface and the tip were calculated for a fixed distance between the tip apex atom and surface atoms. Other atoms were allowed to relax.

The Si tip was modelled according to a T4 tip, an adatom type of tip consisting of 10 Si atoms and 15 hydrogen atoms, which saturate silicon dangling bonds.[64] The graphene sheet model was a 6 × 6 supercell (72 carbon atoms) with a calculated C–C bond length of 1.44 Å. The periodically repeated sheets were separated by at least 20 Å of vacuum. The selection of a suitable graphene oxide model was more complicated. A single O atom adsorbs dominantly onto the bridge site between two C atoms on graphene, producing an epoxy group. With increasing coverage, it has been calculated theoretically that O adatoms tend to form compact islands and a particularly favorable adsorption structure is obtained with an O coverage of 0.5 monolayers.[65] Therefore, we chose to use the latter GO model.

SiO_2 was used as the experimental reference since alpha quartz is the most stable polymorph of silica (SiO_2) under ambient conditions and the (0001) surface is its most stable surface. However, previous MD calculations have shown that the ideal (0001) surface with its high surface energy undergoes reconstruction. Therefore, we simulated annealing by performing *ab initio* MD simulation of a perfect surface at a temperature of 500 K for 2 ps (2000 iterations), followed by relaxation of the resulting surface. The surface energy of the reconstructed surface was 0.6 J m^{-2}, in agreement with previous studies.[45]

Preparation of graphene samples

The single layer graphene flakes were exfoliated according to the Scotch tape method from highly oriented pyrolytic graphite (HOPG). The use of "easy-removable" Scotch tape helps to minimize glue residues. During exfoliation, the tape was

repeatedly folded back on itself until the carbon formed a homogeneous, silver-gray film. The carbon particles were then transferred to the silicon dioxide substrate by gently pressing the tape onto the substrate. From our experience, the yield of single layer graphene by this approach is only a few percent, but it is of very good quality, as both the AFM and XPS results confirmed (Fig. 2 and 3). More details regarding the sample preparation can be found in the ESI.†

Graphene oxidation

The as-prepared graphene flakes were treated in a UV/ozone cleaner from BioForce, which allowed observation of changes induced to the same single flake during treatment. Other advantages of this approach over wet chemical methods are that it is less harsh and produces less chemical waste.[42,66,67] During the functionalization, high energy photons activate carbon–carbon bonds toward the ozone agent, but they can also release oxygen from graphene[68] and prolonged oxidation causes defects in the flake. The carbon transition from sp^2 to sp^3 can be monitored by Raman spectroscopy by comparing the G and D band of graphene (Fig. S-7 in the ESI†).

AFM method

All the AFM images and force curve measurements were acquired with the PeakForce quantitative nanomechanical mapping mode using a commercial Nanoscope MultiMode VIII (Bruker, Santa Barbara, US) (further details in the ESI†). The scan rate was kept constant at 0.5 Hz per line, whereas the range of the scan was altered between 2 μm, 1 μm, and 0.4 μm to compare the effect of different scanning speeds. Furthermore, the sampling rate was kept constant for all measurements at 2 kHz. The probes used were of the type "ScanAsyst Air" from Bruker, Santa Barbara, with a sharp silicon tip and a spring constant range from 0.2 to 0.8 N m^{-1} from the factory. The cantilever used for the data presented here had a spring constant of 0.57 ± 0.06 N m^{-1}. Other cantilevers, from the same box, had a spring constant between 0.41 N m^{-1} and 0.71 N m^{-1}. Cantilever calibrations regarding deflection sensitivity and spring constant were performed on the SiO_2 substrate in combination with Bruker's "Thermal Tune". To avoid the plastic deformation of the probe the indention force was kept below 0.5 nN and not higher than necessary. The blind estimation method[69] revealed that the probe's apex radius was less than or equal to 20.1 nm, which for an unused probe should be better than 10 nm. Since the probe was not manipulated and was monitored during the experiment through its adhesive behavior, the probe could be considered a constant factor. It is very important to maintain the experimental conditions. A constant flow of dry nitrogen kept the humidity at 30% to reduce the effect of hydrophilic materials (further details in the ESI†), such as graphene oxide, which are known to change the force interaction behavior with the probe depending on the humidity.[70]

Conclusions

We employed both experimental and theoretical methods to study changes in the topography and chemical composition induced by oxidation of a single graphene flake. Our DFT calculations revealed that the Si tip–surface interaction was dominated by non-covalent van der Waals forces for both graphene and GO, which explains the modest difference in their adhesion forces observed in the experiment. We directly monitored the gradual process of graphene oxidation by UV/ozone with AFM based dynamic force measurements at the nanoscale resolution under ambient conditions. Using this approach, changes in the chemical functionality of the surface could be mapped alongside topography. The mapping of interaction forces was sensitive enough to distinguish degrees of oxidation and the expansion of higher oxidation starting at the edge of the graphene flake. The susceptibility of graphene edges to oxidation was corroborated by MD simulation. In addition, the contrast in adhesion between the flake and substrate was inverted as a consequence of the oxidation treatment, in accordance with our DFT simulation. This approach can be extended to probe the chemical functionalization of other two-dimensional materials, such as transition metal dichalcogenides, carbon-based materials and flake-substrate composites.

Acknowledgements

The authors gratefully acknowledge support from the Ministry of Education, Youth and Sports of the Czech Republic (projects LO1305 and CZ.1.05/2.1.00/19.0377; and the Research Infrastructure NanoEnviCz under Project No. LM2015073). Michal Otyepka acknowledges support from the Czech Grant Agency (project P208/12/G016), Neuron fund for support of science and H2020 ERC Consolidator grant 683024 (2dchem.org). Jens P. Froning and Martin Pykal were supported by student projects IGA_PrF_2016_021 and IGA_PrF_2016_028 of Palacký University.

References

1 K. S. Novoselov, A. K. Geim, S. V. Morozov, D. Jiang, Y. Zhang, S. V. Dubonos, I. V. Grigorieva and A. A. Firsov, *Science*, 2004, **306**, 666–669.
2 K. S. Novoselov, A. K. Geim, S. V. Morozov, D. Jiang, M. I. Katsnelson, I. V. Grigorieva, S. V. Dubonos and A. A. Firsov, *Nature*, 2005, **438**, 197–200.
3 K. K. Gomes, W. Mar, W. Ko, F. Guinea and H. C. Manoharan, *Nature*, 2012, **483**, 306–310.
4 C. Berger, Z. M. Song, T. B. Li, X. B. Li, A. Y. Ogbazghi, R. Feng, Z. T. Dai, A. N. Marchenkov, E. H. Conrad, P. N. First and W. A. de Heer, *J. Phys. Chem. B*, 2004, **108**, 19912–19916.
5 L. Britnell, R. V. Gorbachev, R. Jalil, B. D. Belle, F. Schedin, A. Mishchenko, T. Georgiou, M. I. Katsnelson, L. Eaves,

S. V. Morozov, N. M. R. Peres, J. Leist, A. K. Geim, K. S. Novoselov and L. A. Ponomarenko, *Science*, 2012, **335**, 947–950.
6 J. N. Tiwari, V. Vij, K. C. Kemp and K. S. Kim, *ACS Nano*, 2016, **10**, 46–80.
7 X. C. Dong, H. Xu, X. W. Wang, Y. X. Huang, M. B. Chan-Park, H. Zhang, L. H. Wang, W. Huang and P. Chen, *ACS Nano*, 2012, **6**, 3206–3213.
8 E. Yoo, J. Kim, E. Hosono, H.-s. Zhou, T. Kudo and I. Honma, *Nano Lett.*, 2008, **8**, 2277–2282.
9 Z. S. Wu, W. C. Ren, L. Wen, L. B. Gao, J. P. Zhao, Z. P. Chen, G. M. Zhou, F. Li and H. M. Cheng, *ACS Nano*, 2010, **4**, 3187–3194.
10 V. Georgakilas, J. N. Tiwari, K. C. Kemp, J. A. Perman, A. B. Bourlinos, K. S. Kim and R. Zbořil, *Chem. Rev.*, 2016, **116**, 5464–5519.
11 H. Tanaka, S. Obata and K. Saiki, *Chem. Lett.*, 2014, **43**, 328–330.
12 K. Erickson, R. Erni, Z. Lee, N. Alem, W. Gannett and A. Zettl, *Adv. Mater.*, 2010, **22**, 4467–4472.
13 S. Park, J. H. An, I. W. Jung, R. D. Piner, S. J. An, X. S. Li, A. Velamakanni and R. S. Ruoff, *Nano Lett.*, 2009, **9**, 1593–1597.
14 Z. J. Wang, X. Z. Zhou, J. Zhang, F. Boey and H. Zhang, *J. Phys. Chem. C*, 2009, **113**, 14071–14075.
15 L. Kou, H. K. He and C. Gao, *Nano-Micro Lett.*, 2010, **2**, 177–183.
16 V. Chandra, J. Park, Y. Chun, J. W. Lee, I.-C. Hwang and K. S. Kim, *ACS Nano*, 2010, **4**, 3979–3986.
17 D. R. Dreyer, S. Park, C. W. Bielawski and R. S. Ruoff, *Chem. Soc. Rev.*, 2010, **39**, 228–240.
18 A. Mokdad, K. Dimos, G. Zoppellaro, J. Tuček, J. A. Perman, O. Malina, K. K. Andersson, K. K. R. Datta, J. P. Froning and R. Zbořil, *RSC Adv.*, 2015, **5**, 76556–76566.
19 H. Zhu, L. Gao, X. Jiang, R. Liu, Y. Wei, Y. Wang, Y. Zhao, Z. Chai and X. Gao, *Chem. Commun.*, 2014, **50**, 3695–3698.
20 Y. Y. Shao, J. Wang, H. Wu, J. Liu, I. A. Aksay and Y. H. Lin, *Electroanalysis*, 2010, **22**, 1027–1036.
21 C. C. Huang, C. Li and G. Q. Shi, *Energy Environ. Sci.*, 2012, **5**, 8848–8868.
22 K. Parvez, S. B. Yang, Y. Hernandez, A. Winter, A. Turchanin, X. L. Feng and K. Mullen, *ACS Nano*, 2012, **6**, 9541–9550.
23 J. M. Yoo, J. H. Kang and B. H. Hong, *Chem. Soc. Rev.*, 2015, **44**, 4835–4852.
24 L. M. Zhang, Y. D. Xing, N. Y. He, Y. Zhang, Z. X. Lu, J. P. Zhang and Z. J. Zhang, *J. Nanosci. Nanotechnol.*, 2012, **12**, 2924–2928.
25 K. K. R. Datta, O. Kozák, V. Ranc, M. Havrdová, A. B. Bourlinos, K. Šafářová, K. Holá, K. Tománková, G. Zoppellaro, M. Otyepka and R. Zbořil, *Chem. Commun.*, 2014, **50**, 10782–10785.
26 S. R. Shin, B. Aghaei-Ghareh-Bolagh, X. Gao, M. Nikkhah, S. M. Jung, A. Dolatshahi-Pirouz, S. B. Kim, S. M. Kim, M. R. Dokmeci, X. Tang and A. Khademhosseini, *Adv. Funct. Mater.*, 2014, **24**, 6136–6144.
27 K. S. Kim, Y. Zhao, H. Jang, S. Y. Lee, J. M. Kim, K. S. Kim, J.-H. Ahn, P. Kim, J.-Y. Choi and B. H. Hong, *Nature*, 2009, **457**, 706–710.
28 V. C. Tung, M. J. Allen, Y. Yang and R. B. Kaner, *Nat. Nanotechnol.*, 2009, **4**, 25–29.
29 X. Li, W. Cai, J. An, S. Kim, J. Nah, D. Yang, R. Piner, A. Velamakanni, I. Jung, E. Tutuc, S. K. Banerjee, L. Colombo and R. S. Ruoff, *Science*, 2009, **324**, 1312–1314.
30 A. Y. S. Eng, C. K. Chua and M. Pumera, *Nanoscale*, 2015, **7**, 20256–20266.
31 N. Lu, D. Yin, Z. Y. Li and J. L. Yang, *J. Phys. Chem. C*, 2011, **115**, 11991–11995.
32 H. C. Schniepp, J. L. Li, M. J. McAllister, H. Sai, M. Herrera-Alonso, D. H. Adamson, R. K. Prud'homme, R. Car, D. A. Saville and I. A. Aksay, *J. Phys. Chem. B*, 2006, **110**, 8535–8539.
33 S. Zhang, H. Aslan, F. Besenbacher and M. Dong, *Chem. Soc. Rev.*, 2014, **43**, 7412–7429.
34 M. H. Whangbo, G. Bar and R. Brandsch, *Surf. Sci.*, 1998, **411**, L794–L801.
35 R. W. Stark, *Mater. Today*, 2010, **13**, 24–32.
36 D. D. Kulkarni, S. Kim, M. Chyasnavichyus, K. Hu, A. G. Fedorov and V. V. Tsukruk, *J. Am. Chem. Soc.*, 2014, **136**, 6546–6549.
37 Y. H. Ding, P. Zhang, H. M. Ren, Q. Zhuo, Z. M. Yang, X. Jiang and Y. Jiang, *Appl. Surf. Sci.*, 2011, **258**, 1077–1081.
38 S. Zhang, F. L. Bach-Gansmo, D. Xia, F. Besenbacher, H. Birkedal and M. Dong, *Nano Res.*, 2015, **8**, 3250–3260.
39 D. Xia, S. Zhang, J. Ø. Hjortdal, Q. Li, K. Thomsen, J. Chevallier, F. Besenbacher and M. Dong, *ACS Nano*, 2014, **8**, 6873–6882.
40 B. Pittenger and A. Slade, *Microsc. Today*, 2013, **21**, 12–17.
41 H. H. Tao, J. Moser, F. Alzina, Q. Wang and C. M. Sotomayor-Torres, *J. Phys. Chem. C*, 2011, **115**, 18257–18260.
42 N. Leconte, J. Moser, P. Ordejón, H. Tao, A. Lherbier, A. Bachtold, F. Alsina, C. M. Sotomayor Torres, J.-C. Charlier and S. Roche, *ACS Nano*, 2010, **4**, 4033–4038.
43 P. Lazar, S. Zhang, K. Šafářová, Q. Li, J. P. Froning, J. Granatier, P. Hobza, R. Zbořil, F. Besenbacher, M. D. Dong and M. Otyepka, *ACS Nano*, 2013, **7**, 1646–1651.
44 M. Ondráček, P. Pou, V. Rozsíval, C. González, P. Jelínek and R. Pérez, *Phys. Rev. Lett.*, 2011, **106**, 176101.
45 T. P. M. Goumans, A. Wander, W. A. Brown and C. R. A. Catlow, *Phys. Chem. Chem. Phys.*, 2007, **9**, 2146–2152.
46 K. L. Johnson, K. Kendall and A. D. Roberts, *Proc. R. Soc. London, Ser. A*, 1971, **324**, 301–313.
47 B. V. Derjaguin, V. M. Muller and Y. P. Toporov, *J. Colloid. Interface Sci.*, 1975, **53**, 314–326.
48 D. Tabor, *J. Colloid. Interface Sci.*, 1977, **58**, 2–13.
49 D.-e. Jiang, B. G. Sumpter and S. Dai, *J. Chem. Phys.*, 2007, **126**, 134701.
50 P. Lazar, E. Otyepková, P. Banáš, A. Fargašová, K. Šafářová, L. Lapčík, J. Pechoušek, R. Zbořil and M. Otyepka, *Carbon*, 2014, **73**, 448–453.

51 X. R. Wang, X. L. Li, L. Zhang, Y. Yoon, P. K. Weber, H. L. Wang, J. Guo and H. J. Dai, *Science*, 2009, **324**, 768–771.
52 S. Park, D. Srivastava and K. Cho, *Nano Lett.*, 2003, **3**, 1273–1277.
53 I. P. Lisovskii, V. G. Litovchenko and V. B. Lozinskii, *Appl. Surf. Sci.*, 1995, **86**, 299–302.
54 M. Kozlowska, J. Goclon and P. Rodziewicz, *Appl. Surf. Sci.*, 2016, **362**, 1–10.
55 K. Chenoweth, A. C. T. van Duin and W. A. Goddard, *J. Phys. Chem. A*, 2008, **112**, 1040–1053.
56 A. Bagri, C. Mattevi, M. Acik, Y. J. Chabal, M. Chhowalla and V. B. Shenoy, *Nat. Chem.*, 2010, **2**, 581–587.
57 S. Plimpton, *J. Comput. Phys.*, 1995, **117**, 1–19.
58 P. E. Blöchl, *Phys. Rev. B: Condens. Matter*, 1994, **50**, 17953–17979.
59 G. Kresse and D. Joubert, *Phys. Rev. B: Condens. Matter*, 1999, **59**, 1758–1775.
60 J. Klimeš, D. R. Bowler and A. Michaelides, *Phys. Rev. B: Condens. Matter*, 2011, **83**, 195131.
61 M. Pykal, P. Jurečka, F. Karlický and M. Otyepka, *Phys. Chem. Chem. Phys.*, 2016, **18**, 6351–6372.
62 P. Lazar, J. Martincová and M. Otyepka, *Phys. Rev. B: Condens. Matter*, 2015, **92**, 224104.
63 P. Lazar, F. Karlický, P. Jurečka, M. Kocman, E. Otyepková, K. Šafářová and M. Otyepka, *J. Am. Chem. Soc.*, 2013, **135**, 6372–6377.
64 P. Pou, *Nanotechnology*, 2009, **20**, 264015.
65 Ž. Šljivančanin, A. S. Milošević, Z. S. Popović and F. R. Vukajlović, *Carbon*, 2013, **54**, 482–488.
66 A. I. Aria, A. W. Gani and M. Gharib, *Appl. Surf. Sci.*, 2014, **293**, 1–11.
67 J. Yuan, L.-P. Ma, S. Pei, J. Du, Y. Su, W. Ren and H.-M. Cheng, *ACS Nano*, 2013, **7**, 4233–4241.
68 P. Kumar, K. S. Subrahmanyam and C. N. R. Rao, *Int. J. Nanosci.*, 2011, **10**, 559–566.
69 J. S. Villarrubia, *J. Res. Natl. Inst. Stand. Technol.*, 1997, **102**, 425–454.
70 A. Ptak, H. Gojzewski, M. Kappl and H. J. Butt, *Chem. Phys. Lett.*, 2011, **503**, 66–70.